

Chapter 2

Experimental Observations

*An experiment is a device to make Nature speak intelligibly.
After that one has only to listen.*

George Wald [2.1]

Abstract Starting points for getting acquainted with the phenomena of dissipative solitons are chemical reaction diffusion systems and a planar semiconductor-gas-discharge system. These systems exhibit dissipative solitons in the form of self-organized localized concentration spots and current density filaments, respectively. The chapter discusses the experiments and concentrates on the phenomena being directly related to the particle-like characteristics of dissipative solitons in spatially extended systems. These are the dynamics of single dissipative solitons, their mutual interaction by scattering and formation of bound states, as well as generation and annihilation processes. Due to the focus of the book, only continuously driven experiments are considered.

2.1 Chemical Systems

2.1.1 Overview

Since the first successful experimental realization of Turing patterns in a reaction-diffusion system in the beginning of the 1990s, which was undertaken by de Kepper and coworkers in the chlorite-iodate-malonic-acid (CIMA) system [2.2], the number of systems showing stationary patterns has increased significantly and the focus of research has changed to the control of spatio-temporal structure formation [2.3,2.4]. Nearly at the same time another important experimental observation was reported, namely the self-organization of localized concentration spots in a surface reaction [2.5]. These dissipative solitons propagate in a lateral extended system and interact

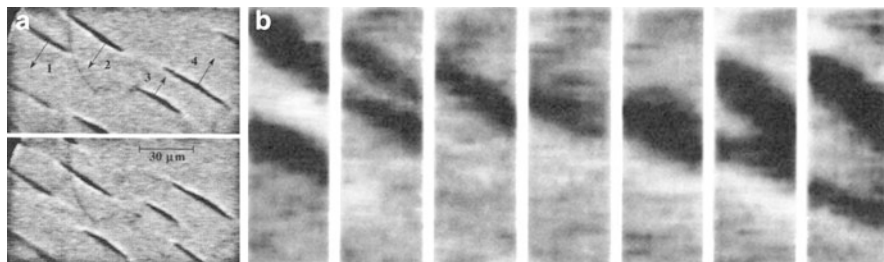


Fig. 2.1 Propagating and interacting dissipative solitons observed as concentration peaks of atomic oxygen adsorbed on the (110) face of a platinum crystal under steady-state conditions of catalytic CO oxidation. Regions with increased oxygen concentration appear *dark*. (a) Two PEEM images recorded with a time interval of 3.0 s from a $130 \times 70 \mu\text{m}^2$ -region of the crystal, (b) sequence of seven PEEM images recorded with a time interval of 1.1 s from a $10 \times 30 \mu\text{m}^2$ slice showing the merging and splitting of two interacting dissipative solitons. Parameters: $p_{\text{O}_2} = 35 \text{ mPa}$, $p_{\text{CO}} = 10 \text{ mPa}$, $T = 485 \text{ K}$, $t_{\text{exp}} = 20 \text{ ms}$ (Reprinted figure with permissions from [2.5])

in a characteristic way with each other (Sect. 2.1.2). However, although the majority of papers on structure formation in chemical systems consider spatially extended systems, reports on dissipative solitons in these systems are rarely found. The reason is twofold: In the case of the dissipative solitons observed in the ferrocyanide-iodate-sulphite reaction [2.6] some experimental details were not obvious and it took more than a decade to reproduce the original observations (Sect. 2.1.5). In the majority of other systems an external stabilization is either needed in the form of an external feedback (Sect. 2.1.3) or by boundary conditions, e.g., by constraining the active area to a ring-like geometry [2.7]. In the latter scenario the resulting dissipative solitons are comparable to nerve pulses (Fig. 1.1c), which have only one degree of freedom and therefore can only interact with each other in a very confined way. A completely different approach for stabilizing dissipative solitons in spatially extended reaction-diffusion systems has been demonstrated by the Brandeis group, which performs the Belousov-Zhabotinsky reaction in nano structured batch reactors (Sect. 2.1.4).

2.1.2 Catalytic Oxidation of CO on Pt(110)

The first dissipative solitons to be observed in a spatially extended reaction-diffusion system have been reported by Rotermund et al. [2.5]. They conducted experiments on the catalytic oxidation of carbon monoxide on the (110) face of a single crystal of platinum placed inside an ultra high vacuum system and monitored the experiment with a photoemission electron microscope (PEEM) [2.8]. The image contrast of this microscope results from the different dipole moments of the adsorbate complexes O_{ad} and CO_{ad} , such that oxygen covered areas appear dark, while those covered by CO are gray (Fig. 2.1). In particular, Rotermund et al. observed concentration

peaks of atomic oxygen propagating with a uniform velocity of $3.2 \pm 0.2 \mu\text{m/s}$ along the crystallographic (100) direction of the Pt(110) substrate. These dissipative solitons exhibit a characteristic bell-shaped intensity profile, which is elongated perpendicular to the direction of motion (Fig. 2.1a).

Due to their parallel direction of motion only head-on collisions between dissipative solitons are observed which normally lead to the extinguishing of one of the dissipative solitons. However, one also observes the mutual annihilation of both dissipative solitons or the merging and subsequent splitting of the intermediate state (Fig. 2.1b).

Since the first reports of this phenomenon, the investigations on dissipative solitons on excitable surface reactions have been quite extended, such that a huge variety of additional phenomena like the refraction of dissipative solitons crossing the border from a domain consisting of pure platinum to a gold covered platinum domain [2.9], the merging of two dissipative solitons to a single one in the course of the catalytic reduction of NO with CO on a Pt(110) surface [2.10] or the propagation of dissipative solitons on polycrystalline platinum under atmospheric pressure [2.11] have been reported.

2.1.3 The Belousov-Zhabotinsky Reaction

The most important chemical reaction for the invention of self-organized spatio-temporal dynamics has been discovered in the 1950s by Belousov [2.12]. He observed that in a closed system the cerium-catalyzed bromate oxidation of citric acid undergoes a large number of oscillations before reaching thermodynamic equilibrium. Later on Zhabotinsky repeated Belousov's experiments, replacing the citric acid substrate by malonic acid and substituting the oxidation-reduction indicator ferroin (tris(1,10-phenanthroline)iron(II)) for the cerium catalyst, leading to the well-known blue-red colour changes [2.13].

Investigations of the spatio-temporal dynamics of the Belousov-Zhabotinsky (BZ) reaction started in the early 1970s of the last century with the observation of travelling concentration waves in quasi-two-dimensional layers of unstirred BZ reactant mixtures [2.14–2.16]. These waves typically appear in form of blue fronts, targets or spirals (Fig. 1.1h) embedded into the red background of the reduced catalyst. Replacing ferroin by the photosensitive catalyst $\text{Ru}(\text{bipy})_3^{2+}$ (tris(2,2'-bipyridyl)ruthenium(II)) [2.17] opened the way towards controlling pattern formation in the BZ reaction [2.3, 2.4].

The experimental setup is straight forward [2.18, 2.19]: A thin layer of silica gel in which the light sensitive catalyst is immobilized is cast onto a microscope slide and mounted inside of a reactor that is continuously fed with fresh, catalyst-free BZ solution (Fig. 2.2a). Images $\phi(\mathbf{x}, t)$ of the chemical pattern are recorded by a CCD camera and are converted into a feedback signal in form of an $30 \times 20 \text{ mm}^2$ image, which is projected through a 460 nm bandpass filter onto the gel. Because the excitability of the medium decreases with increasing light intensity the feedback

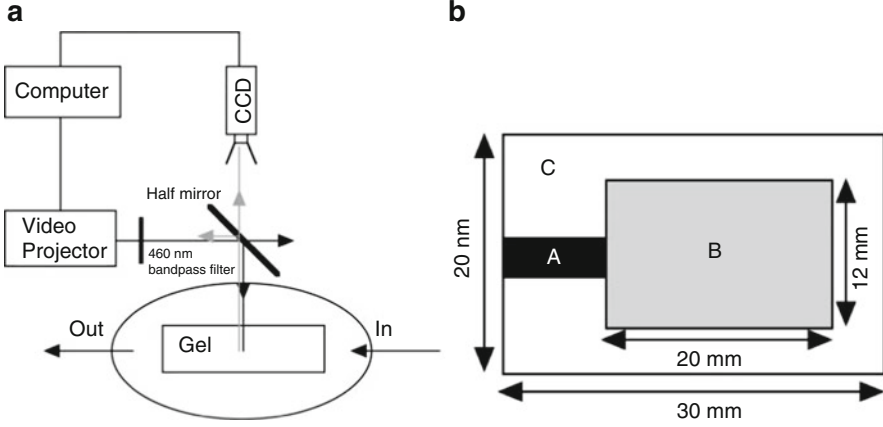


Fig. 2.2 Experimental setup for the observation of dissipative solitons in the BZ reaction [2.18]. (a) The feedback is realized as computer generated image being projected onto the reactor. (b) The feedback image consists of an initiation zone (A), a reaction zone (B) with adapted gray level, and a surrounding boundary (C) which confines the dissipative solitons. Typical parameters of the experiment are given in Fig. 2.3

image consists of three different zones (Fig. 2.2b): a dark initiation zone (label A), a reaction zone of $20 \times 12 \text{ mm}^2$ with adapted gray level (label B), and a boundary with high intensity (label C). The dissipative solitons are initiated in the dark zone and are allowed to propagate into the reaction zone, to which they are confined due to the high intensity of the boundary zone. The gray-level of the reaction-zone is chosen proportional to the area covered by the observed dissipative soliton, such that the illumination intensity $\Phi(t)$ of the reaction zone is given by

$$\Phi(t + \Delta t) = \kappa_1 + \kappa_2 \int_{\{x | \phi(x,t) \geq \phi_T\}} \phi(x, t) dx. \quad (2.1)$$

Here parameter κ_1 determines the offset illumination within the reaction zone, κ_2 is the feedback parameter, and ϕ_T is the threshold used for separating the localized structure from the homogeneous background.

The experiments show, that self-organized localized structures form which are not confined by the boundary of the reaction zone but exhibit a well defined shape that is elongated perpendicular to the direction of motion (Fig. 2.3). Varying the feedback parameter κ_1 reveals, that the size of the dissipative solitons decreases with increasing illumination parameter κ_1 . This is due to the fact, that a higher illumination intensity excites a larger amount of the ruthenium catalyst, leading to an increased reaction rate of the excited catalyst with bromomalonic acid. This reaction produces bromide, which acts as inhibitor for the autocatalysis [2.17]. The same mechanism controls the size of the dissipative solitons, because a small increase of its shape would lead via the feedback loop (2.1) to an increase of the illumination

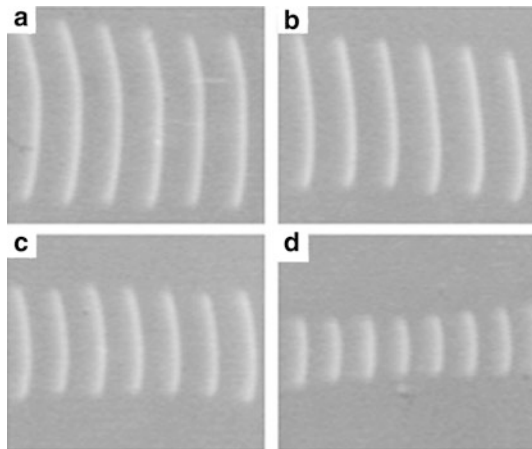


Fig. 2.3 Propagating dissipative solitons in a photosensitive BZ-medium with optical feedback [2.18]. The images show, that the size of the dissipative solitons decrease with increasing illumination intensity (2.1) (a) $\kappa_1 = -0.0744 \text{ mW/cm}^2$, (b) $\kappa_1 = -0.0248 \text{ mW/cm}^2$, (c) $\kappa_1 = 0.0248 \text{ mW/cm}^2$, (d) $\kappa_1 = 0.0744 \text{ mW/cm}^2$. The interval between the superimposed snapshots is 40 s. Composition of catalyst free BZ-solution: $[\text{NaBrO}_3]_0 = 0.28 \text{ M}$, malonic acid $[\text{MA}]_0 = 0.05 \text{ M}$, bromomalonic acid $[\text{BrMA}]_0 = 0.165 \text{ M}$, sulfuric acid $[\text{H}_2\text{SO}_4]_0 = 0.36 \text{ M}$. The silica gel medium ($0.3 \times 20 \times 30 \text{ mm}^3$) was prepared by acidifying an aqueous solution of 10 % (w/w) Na_2SiO_3 and $2.0 \text{ mM Ru}(\text{bpy})_3^{2+}$ with H_2SO_4 . Temperature $T = 9.0^\circ\text{C}$, displayed area $7.78 \times 6.53 \text{ mm}^2$. Feedback: $\Delta t = 2 \text{ s}$, $\kappa_2 = 37.5 \text{ mW/cm}^4$, $\phi_T = 1.1 \langle \phi(x, t) \rangle_x$. For additional parameters see [2.18]

and a reduced excitability of the active medium. On the other hand a small decrease of its shape would lead to a decrease of the illumination and an increased excitability allowing for the growth of the dissipative soliton.

On basis of this experimental setup it has been shown, that dissipative solitons can form due to stochastic resonance [2.20], exhibit oscillatory cluster patterns [2.21], and are propelled in unexcitable BZ-media by periodic forcing [2.22]. It has also been demonstrated, that dissipative solitons can be guided on complex paths [2.23] and can interact via interaction potentials superimposed to the illumination mask [2.24, 2.25].

2.1.4 The Belousov-Zhabotinsky-Aerosol OT-Microemulsion System

The fact, that the BZ reaction is capable of showing spatio-temporal structure formation raises the question, whether this system is capable of developing periodic patterns. These so-called Turing patterns need two requirements: A continuous flow of matter and an inhibitor diffusing faster than the activator [2.26]. The first condition has been realized in the late 1980s by the invention of the continuously fed unstirred reactor (CFUR) [2.27]. The second condition was first realized,

not in the BZ reaction, but in the chlorite-iodide-malonic acid (CIMA) reaction [2.2, 2.28, 2.29]. These experiments were carried out in a gel CFUR allowing for a continuous supply of fresh reactants. Furthermore de Kepper et al. used starch as indicator, which forms a reversible complex with iodide, the activator for the autocatalytic reaction, and iodine, an intermediate produced in the reaction. Due to their size, these complexes stuck every now and then in the pores of the gel, which effectively reduces the diffusion rate of the activator. On the other hand the inhibitor, chlorite, can diffuse unhindered through the gel, leading to significantly larger diffusion rates compared to the activator and thus fulfilling Turing's condition [2.4].

In an aqueous solution of a typical BZ-reaction the diffusion rates of the activator, the radical BrO_2^\bullet , and the inhibitor, Br_2 , are all on the order of $2 \cdot 10^{-5} \text{ cm}^2 \text{ s}^{-1}$, thus Turing patterns cannot form. An answer to this problem has been found by Vanag and Epstein, who mixed the BZ reactants with a reverse microemulsion of water, oil, and the surfactant sodium bis(2-ethyl-hexyl)sulfosuccinate, the so-called aerosol OT (AOT), realizing the BZ-AOT reaction [2.30]. The reverse microemulsion consists of droplets of water surrounded by a monolayer of AOT floating in a sea of oil. The water droplets of this ternary mixture have a diameter of several nanometers and diffuse with a rate of $(10^{-6} - 10^{-7}) \text{ cm}^2 \text{ s}^{-1}$ [2.4]. Because the polar species and thus the activator are mainly confined to the water droplets, while for certain conditions the dominant species of the oil phase is the inhibitor Br_2 , which diffuses with a rate of $2 \cdot 10^{-5} \text{ cm}^2 \text{ s}^{-1}$, the inhibitor diffuses 10–100 times faster than the activator allowing for the formation of Turing-patterns [2.30]. Having in mind that the BZ reaction involves at least ten different reactions [2.31], which are reduced to five chemical steps in the Oregonator model [2.32], it becomes clear that the given description of the BZ-AOT reaction is quite simplified. Therefore additional mechanisms like the effect of a second fast diffusing activator are considered in order to interpret phenomena like accelerating waves [2.30]. A comprehensive overview of the phenomena observed in the BZ-AOT system can be found in [2.33].

In order to observe structure formation phenomena in the BZ-AOT system the microemulsion is prepared as a 1.5 M solution of AOT in octane. One part of the microemulsion is mixed with aqueous solutions of H_2SO_4 and malonic acid and the second part is mixed with aqueous solutions of the catalyst and sodium bromate. Equal volumes of each microemulsion are mixed and filled into a cylindrical batch reactor of diameter 20 mm and height 0.1 mm. This reaction layer is illuminated by a 40 W tungsten lamp whose light is filtered by a 450 nm interference filter. The patterns forming in the reactive layer are observed by a CCD camera. Due to the batch configuration the pattern typically persists for 1–3 h.

Two important control parameters determine the structure formation of the system: The droplet fraction and the reactivity. Both parameters cannot be tuned within a running experiment but can be varied from experiment to experiment. An overview of the experimental phenomena observed for varied droplet fraction and varied reactivity is shown in [2.30, 2.33]. The droplet fraction is directly related to the diffusion rates of the chemical species and increasing the droplet fraction basically leads to a transition from stationary to dynamic structures. On the other hand the excitability of the BZ-AOT system results from the ratio

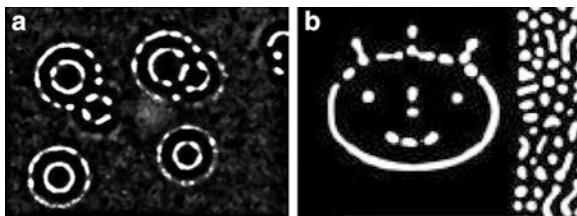


Fig. 2.4 Dissipative solitons in the BZ-AOT reaction. *White areas correspond to a large concentration of the oxidized catalyst ($\text{Ru}(\text{bpy})_3^{2+}$).* (a) Self-organized rings. (b) Structures initialized by inhomogeneous illumination. Parameters: (a) Composition of aqueous BZ-solution: $[\text{NaBrO}_3]_0 = 0.2 \text{ M}$, malonic acid $[\text{MA}]_0 = 0.25 \text{ M}$, catalyst $[\text{Ru}(\text{bpy})_3^{2+}]_0 = 4.2 \text{ mM}$, sulfuric acid $[\text{H}_2\text{SO}_4]_0 = 0.25 \text{ M}$. Droplet fraction $\varphi_d = 0.41$, temperature $T = 23.5^\circ\text{C}$, displayed area $5.1 \times 3.75 = \text{mm}^2$, for additional parameters see [2.36]. (b) Composition of aqueous BZ-solution: $[\text{NaBrO}_3]_0 = 0.25 \text{ M}$, malonic acid $[\text{MA}]_0 = 0.1 \text{ M}$, catalyst $[\text{Ru}(\text{bpy})_3^{2+}]_0 = 4.0 \text{ mM}$, sulfuric acid $[\text{H}_2\text{SO}_4]_0 = 0.3 \text{ M}$. Droplet fraction $\varphi_d = 0.45$, initial illumination intensity $I_0 = 28 \text{ mW/cm}^2$, illumination intensity after removing the mask $I = I_0/5$, temperature $T = 24.0^\circ\text{C}$, displayed area $7.7 \times 5.8 = \text{mm}^2$, for additional parameters see [2.35]. Figures published with kind permission of I.R. Epstein

between activation and inhibition steps, which can be parameterized by the ratio $\sigma_{\text{BZ}} = [\text{H}_2\text{SO}_4][\text{NaBrO}_3]/[\text{MA}]$ [2.33]. While the monotonic state of the system is stable for small values of σ_{BZ} , one observes spontaneous formation of stationary structures for $0.01 < \sigma_{\text{BZ}} < 0.09$ and complex spatio-temporal dynamics for larger values of σ_{BZ} [2.33, Fig. 5.3].

Dissipative solitons in form of localized stationary structures can be observed in the BZ-AOT system close to the transition from the monotonic to the periodically structured state (Fig. 2.4). They are observed as regions of locally increased concentration of the reduced catalyst taking the form of spots, concentric rings, or strings of well-defined width. In any case, the dissipative solitons have to be created by some kind of finite perturbation. This might be either dust particles [2.34] triggering the formation of concentric rings (Fig. 2.4a) or an inhomogeneous illumination. In the example shown in Fig. 2.4b the inhomogeneous illumination has been realized as a mask showing a smiley and a vertical bar [2.35]. Due to the light sensitivity of the catalyst, the masked regions exhibit a larger reactivity, leading to the spontaneous formation of a Turing-pattern in the region masked by the vertical bar as well as localized spots and strings of well-defined width in the regions shaded by the smiley mask. After removing the mask, the self-organized structures persist up to an hour, while the strings decompose into chains of localized spots still resembling an outline of the initial image. The vanishing of the localized structures is caused by consumption of the reactants due to the batch configuration of the experiment.

As mentioned above the BZ-AOT system exhibits complex spatio-temporal dynamics for larger values of σ_{BZ} . In contrast to the well-known phenomena of autowaves or spirals known from other reaction-diffusion systems, some of the corresponding structures observed in the BZ-AOT system are segmented. For example

one observes dash waves, segmented circular waves, segmented spirals, and fronts of bubbles [2.33]. From these observations one might suggest that the BZ-AOT system is a promising candidate for investigating the interaction of dissipative solitons in chemical reaction-diffusion systems without applying an artificial interaction by inhomogeneous illumination. In the BZ-AOT system such experiments could be prepared by initiating two or more dissipative solitons due to a transient inhomogeneous illumination similar to the example discussed in Fig. 2.4a. After removing the mask, the temperature of the system could be increased in order to increase the reactivity of system, which might lead to a drift-bifurcation of the dissipative solitons.

2.1.5 *Ferrocyanide-Iodate-Sulphite (FIS) Reaction*

From the historical point of view, the first oscillating chemical reaction showing dissipative solitons in form of localized concentration spots is the ferrocyanide-iodate sulphite (FIS) reaction [2.6]. The autocatalytic mechanism of this reaction is the hydrogen ion driven oxidation of hydrogen sulfite, which is inhibited by the hydrogen ion consuming oxidation of ferrocyanide. Therefore the spatial structures of the system can be easily visualized by using a pH indicator. Because the FIS reaction only oscillates in an open system, the continuous supply of reactants has to be provided by using a continuously stirred tank reactor (CSTR) [2.37], which was invented for generating Turing patterns in the CIMA reaction [2.38]. In the original setup of the Austin group, the reactor consists of a thin poly(acrylamide) gel layer of width $d = 0.2$ mm and diameter $D = 22$ mm which is fed via diffusion by the reactants from the reservoir [2.6, 2.37].

From theoretical considerations it is well known that the diffusivity of the autocatalytic species needs to be smaller than the diffusivity of the inhibitory species in order to obtain stationary self-organized patterns [2.26]. Though this topic has not been considered in the original papers of the Austin group recent investigations show that a critical concentration of weak acid functions with low mobility is needed in order to observe stationary reaction-diffusion patterns in the FIS reaction [2.39, 2.40]. Due to the fast protonation equilibrium, these functions considerably decrease the diffusivity of the hydrogen ions. In the experiments of Szalai and de Kepper this condition is realized by impregnating a disk of agarose gel with 20 mM poly(acrylate). The authors of these recent investigations assume that the same condition was realized in the original experiments of the Austin group by the hydrolysis of the poly(acrylamide) gel due to the degradation of amide functions to carboxylate functions in alkaline aqueous solutions.

In both cases the reactor is illuminated with orange light and concentrations spots of high pH are indicated by bromothymol blue, which changes from yellow to blue as the pH increases from 6.0 to 7.6. While the first report on stationary patterns in the FIS reaction discussed lamellar structures resulting from front-front interactions [2.37], a later paper [2.6] shows that increasing the concentration of ferrocyanide beyond the lamellar regime leads to the formation of concentrations spots of low pH, which undergo a subsequent process of replication by division (self-replication) and

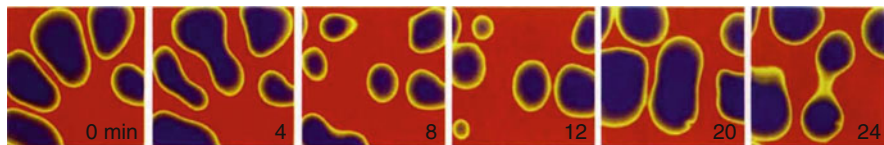


Fig. 2.5 Self-replication of dissipative solitons observed in the ferrocyanide-iodate-sulphite reaction. *Blue* and *red* regions represent states of high and low pH, respectively. The false colour representation has been created from grayscale images recorded in reflected light with a CCD camera. Concentrations of reagents fed in the reservoir of the reactor: $[\text{NaIO}_3]_0 = 75.0 \text{ mM}$, $[\text{Na}_2\text{SO}_3]_0 = 89.0 \text{ mM}$, sulfuric acid $[\text{H}_2\text{SO}_4]_0 = 3.6 \text{ mM}$, $[\text{NaOH}]_0 = 0.25 \text{ mM}$, $[\text{K}_4\text{Fe}(\text{CN})_6 \cdot \text{H}_2\text{O}]_0 = 36.4 \text{ mM}$. Input flow rate 86.4 ml/h , temperature of the reactor 30°C , edge length of the displayed area $L_d = 7 \text{ mm}$, diameter of the reaction volume $D = 22 \text{ mm}$, height of the reaction volume $d = 0.4 \text{ mm}$, sampling frequency $f_{\text{rep}} = 4 \text{ min}$ (Reprinted by permission from Macmillan Publishers Ltd: Nature [2.42], copyright 1994)

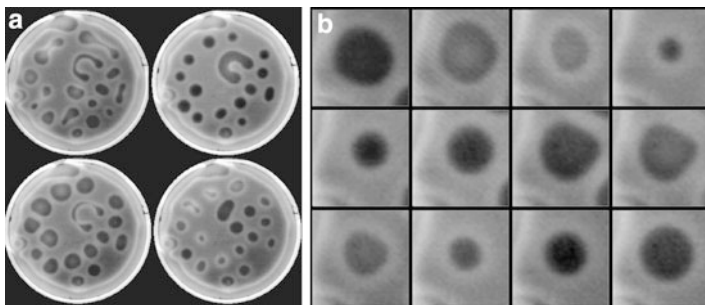


Fig. 2.6 Breathing dissipative solitons in the FIS reaction. *Dark* and *light* regions represent states of high and low pH, respectively. The images have been recorded by a CCD camera from the light transmitted through the reactor. Concentrations of reagents fed in the reservoir of the reactor: $[\text{KIO}_3]_0 = 75.0 \text{ mM}$, $[\text{Na}_2\text{SO}_3]_0 = 89.0 \text{ mM}$, sulfuric acid $[\text{H}_2\text{SO}_4]_0 = 3.09 \text{ mM}$, $[\text{K}_4\text{Fe}(\text{CN})_6 \cdot \text{H}_2\text{O}]_0 = 20.0 \text{ mM}$, $[\text{poly}(\text{acrylate})]_0 = 2.0 \text{ mM}$. Temperature of the reactor 30°C , diameter of the reaction volume $D = 18 \text{ mm}$, height of the reaction volume $d = 0.75 \text{ mm}$, (a) sampling frequency $f_{\text{rep}} = 8 \text{ min}$, (b) sampling frequency $f_{\text{rep}} = 4 \text{ min}$, edge length of the displayed area $L_d = 3.5 \text{ mm}$ (Reprinted with permission from [2.40])

annihilation due to overcrowding (Fig. 2.5). A similar phenomenon is observed for the semiconductor-gas-discharge system (Fig. 2.12) which has been characterized by Astrov and Purwins as spatio-temporal chaos [2.41].

In a subsequent paper the Austin group investigated the spatial bistability of the system systematically by varying the flow rate, the gel thickness, and the concentration of ferrocyanide and reported the observation of breathing domains of low pH concentration and breathing dissipative solitons in the form of high pH concentration spots embedded in a low pH concentration domain [2.43]. After realizing the crucial role of charged polymers for the differentiation between the diffusivity of the activating and the inhibiting species the Bordeaux group investigated the bistability of the spatially extended FIS reactor and repeated the original experiments of breathing dissipative solitons (Fig. 2.6). Furthermore

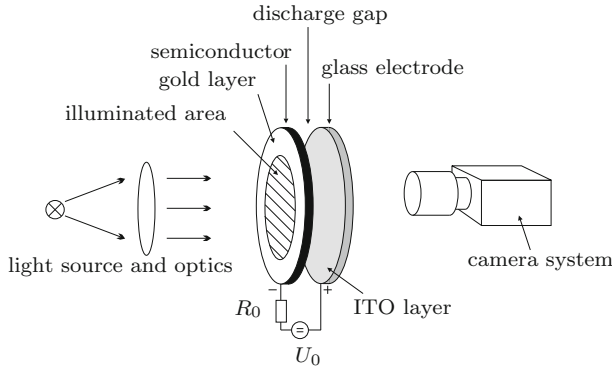


Fig. 2.7 Experimental setup of the semiconductor gas-discharge system [2.52]. The graphics does not show the cryostat, in which the semiconductor electrode is located. Typical parameters of the system are documented in Figs. 2.8–2.20

they investigated the three-dimensional structure of the observed structures and documented the formation of one-dimensional dissipative solitons due to the interaction of reaction fronts [2.40].

It can be expected that after clarifying the experimental details of the FIS reaction, this system will lead to many new experiments on the dynamics of dissipative solitons in chemical reaction-diffusion systems.

2.2 Planar Semiconductor Gas-Discharge Systems

2.2.1 Experimental Set-Up

The experimental system discussed in this section is a variant of the device, which has originally been developed for the fast conversion of infrared light into the visible spectrum [2.44–2.51]. The heart of the experiment is a discharge gap, which is build from two planar electrodes (Fig. 2.7). For the experiments discussed in this book the discharge gap is typically filled with nitrogen at pressure $p_g = 100 - 500$ hPa. One of the electrodes consists of a high ohmic semiconductor like GaAs(Cr), Si(Zn), Si(Pt) or Si(Au) of width $a_{SC} = 0.25 - 1.0$ mm. The other electrode is a glass substrate coated with indium tin oxide (ITO), which is transparent for visible light. The high ohmic electrode is contacted by a gold layer. Typically the high and low ohmic electrodes are wired as cathode and anode, respectively. In some experiments the semiconductor electrode is located inside of a cryostat and is cooled down to $T_{SC} = 100$ K. In contrast to the infrared converter, which typically has a discharge gap of width $d = 0.1$ mm, the pattern forming system has a discharge gap of width $d = 0.4 - 1.4$ mm. The gas discharge system is driven by a DC voltage U_0 . In some experiments the current I in the discharge gap is limited by a series resistor R_0 .

The specific conductivity σ_{SC} of the semiconductor can be controlled by an external light source via the internal photo effect. The diameter of the illuminated semiconductor area is typically $D \approx 20$ mm.

If the applied DC voltage U_0 exceeds a critical value U_c the discharge ignites. Therefore the critical value is called ignition voltage. The emitted light is proportional to the local current density [2.53] and can be observed as luminance distribution $\phi(x, t)$ through the transparent electrode. Of course the luminance can also be recorded by camera systems. Depending on the investigated phenomena the exposure time t_{exp} varies between 0.4 and 20 ms and the sample frequency f_{rep} varies between 50 Hz and 2 kHz. Typical control parameters of the experiment are the supply voltage U_0 and the specific conductivity σ_{SC} of the semiconductor.

This experiment shows a huge variety of different structure formation phenomena, which range from Turing-patterns [2.53–2.55], spirals [2.56], and zigzag destabilized structures [2.57, 2.58] to current density filaments [2.59–2.62] and filament chains [2.63]. Thereby the observed current density filaments exhibit pronounced particle-like properties like their mutual interaction (Sect. 2.2.5) and the generation and annihilation of particles (Sect. 2.2.3). Under certain experimental conditions one can observe an oscillation of the homogeneous background discharge, which triggers an oscillation of the current density filaments [2.64]. However, the following portrayal concentrates on experimental configurations with stationary background discharges.

2.2.2 Observation of Current Density Filaments

Dissipative solitons in form of current density filaments as observed in semiconductor gas-discharge systems are localized three-dimensional structures with two dimensions being given by the lateral expansion of the electrodes and a vertical dimension being given by the finite width of the discharge gap (Fig. 2.7). The structuring of the filaments in the vertical direction becomes more and more complex with increasing discharge gap [2.65, S. 56ff]. The increase of complexity can be explained by the formation of the positive discharge column and Faraday's dark space. However, for most experimental setups the discharge gap d is small compared to the diameter D of the active area ($d/D \approx 10^{-2}$), such that the current density filaments can be regarded as two-dimensional structures. In this case the emitted luminance is integrated over the vertical dimension thus becoming a two-dimensional luminance distribution. Therefore current density filaments are recognized as areas of locally increased luminance typically exhibiting a bell-shaped profile. These solitary objects only exist due to a continuous flow of energy and are classified as *dissipative solitons*.

Because the discharge is disturbed by thermal fluctuations and discharge noise [2.49] the shape of the filaments is noisy, too. However, for experiments without oscillatory instabilities and spatiotemporal uncorrelated noise the fluctuations can be averaged out from a series of snapshots as described by Gurevich et al. [2.66].

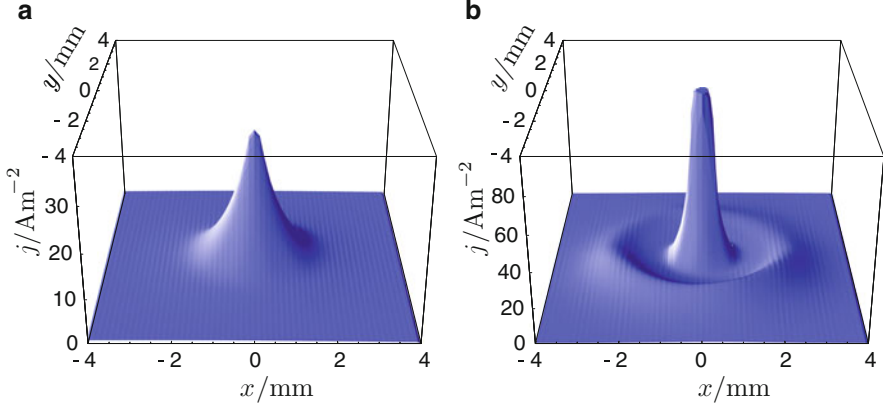


Fig. 2.8 Averaged luminance distribution of dissipative solitons in form of current density filaments [2.52]. **(a)** Current density filament with bell-shaped profile averaged from 1,000 snapshots. **(b)** Current density filament with oscillatory tails averaged from 1,000 snapshots. Parameters: **(a)** $U_0 = 2.74 \text{ kV}$, $\rho_{SC} = 4.95 \text{ M}\Omega \cdot \text{cm}$, $R_0 = 20 \text{ M}\Omega$, $I = 46 \mu\text{A}$, semiconductor GaAs(Cr), $p_{N_2} = 280 \text{ hPa}$, $T_{SC} = 105 \text{ K}$, $D = 17 \text{ mm}$, $d = 250 \mu\text{m}$, $a_{SC} = 1.0 \text{ mm}$, $t_{\text{exp}} = 20 \text{ ms}$, $f_{\text{rep}} = 50 \text{ Hz}$. **(b)** $U_0 = 3.9 \text{ kV}$, $\rho_{SC} = 3.05 \text{ M}\Omega \cdot \text{cm}$, $R_0 = 4.4 \text{ M}\Omega$, $I = 200 \mu\text{A}$, semiconductor GaAs(Cr), $p_{N_2} = 280 \text{ hPa}$, $T_{SC} = 100 \text{ K}$, $D = 17 \text{ mm}$, $d = 500 \mu\text{m}$, $a_{SC} = 1.0 \text{ mm}$, $t_{\text{exp}} = 20 \text{ ms}$, $f_{\text{rep}} = 50 \text{ Hz}$.

An example of a bell-shaped luminance distribution of an experimentally observed filament is shown in Fig. 2.8a. For some experiments this method is also capable of visualizing the oscillatory tails of current density filaments [2.52], which usually are not visible within the background noise. A corresponding example is given in Fig. 2.8b.

2.2.3 Generation and Annihilation Phenomena

The particle-like character of dissipative solitons becomes obvious from the fact, that they are generated or annihilated as a whole. Therefore current density filaments are the smallest elementary building block from which more complex bound or unbound states are formed. In general generation and annihilation phenomena occur either due to a variation of control parameters or due to interaction processes with other dissipative solitons or the domain boundary. In the following sections both scenarios are discussed by means of representative experimental examples.

2.2.3.1 Controlling the Specific Conductivity of the Semiconductor

An important mechanism for generating dissipative solitons is the Turing-mechanism, which is a spatial instability leading to the spontaneous structuring of

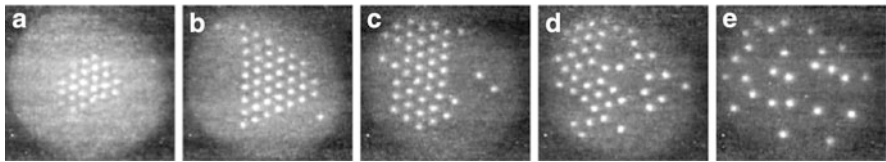


Fig. 2.9 Evolution of a Turing-pattern to an assemble of particle-like structures due to an increase of the specific conductivity of the semiconductor [2.59]. Subfigures (a) and (b) show Turing-patterns with small and large amplitude, respectively. Subfigures (c)–(e) show the dissolving of the hexagonal structure and the transition to a liquid-like state, which is characterized by the mutual interaction of the current density filaments, while a certain short-range order is preserved. In order to realize a high specific resistivity of the Si(Zn)-semiconductor, the system has been cooled down to a temperature of $T_{SC} = 90$ K. The series of images (a)–(e) corresponds to an increase of the specific conductivity of the semiconductor from $\sigma_H = 0.8 \cdot 10^{-8}$ to $4.0 \cdot 10^{-8} (\Omega \text{ cm})^{-1}$, $U_0 = 2.9$ kV, $R_0 = 41$ M Ω , $p_{N_2} = 260$ hPa, $D = 20$ mm, $d = 500$ μ m

the domain (Sect. 3.3.2). In the semiconductor gas-discharge system the Turing-instability can be triggered by a variation of the specific conductivity of the semiconductor as shown by Astrov and Purwins [2.59]. In this experiment the increase of the conductivity destabilizes a homogeneous gas discharge into a hexagonal Turing-pattern with small amplitude (Fig. 2.9a), which evolves into a hexagonal pattern with large amplitude if the specific conductivity of the semiconductor is increased even further (Fig. 2.9b). With ongoing stepwise increase of the control parameter the rigid arrangement of the cluster dissolves, which is accompanied by more and more localized structures dissolving from the cluster (Fig. 2.9c–e). Thereby single current density filaments behave like individual, mutually interacting particles of a liquid state. For example *elastic* scattering between two current density filaments or the formation of transient bound states can be observed [2.59, p. 352], which indicates the existence of a certain short range order between the current density filaments.

The experiment also shows, that the number of current density filaments fluctuates. For example single filaments vanish after collisions with the boundary of the active (illuminated) area of the semiconductor. At the same time the reduction of the number of filaments boosts the generation of new filaments by two- or many-particle-processes (cf. Fig. 2.13).

A completely different phenomena is observed, if the experiment is performed without a series resistor [2.41, Fig. 5]. In this case the global current is not restricted, such that increasing the specific conductivity while keeping the supply voltage fixed leads to an increase of the amplitude of the current density filament. Therefore the spatial period of the pattern grows until the filaments finally become unstable and start to split and merge spontaneously which is characterized as spatio-temporal chaos [2.41].

2.2.3.2 Controlling the Supply Voltage

An important feature of the semiconductor gas-discharge system is its multi-stability, which is reflected by an hysteresis of the current-voltage-characteristics.

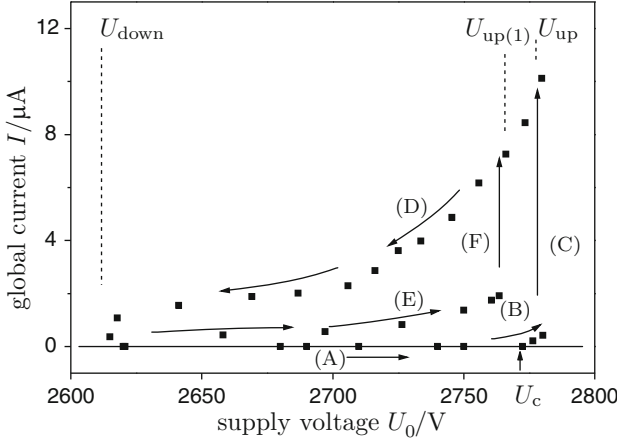


Fig. 2.10 Current-voltage-characteristic of the self-completion scenario [2.55]. Parameters: No series resistor, $p_{N_2} = 168$ hPa, $D = 20$ mm, $d = 1.0$ mm, $a_{SC} = 1.0$ mm

Such kind of hysteresis is e.g. reported by Astrov and Logvin [2.55], who observe the generation of new current-density filaments due to a self-completion scenario. From the theoretical point of view this observation is very important, because it is the experimental evidence of an effect predicted by Gierer and Meinhardt [2.67], which can be regarded as one of the generic mechanisms for generating dissipative solitons (cf. Sect. 7.1.3).

In order to summarize the observation of Astrov and Logvin [2.55] their recorded current-voltage-characteristics is reprinted in Fig. 2.10. Its tags (A)–(F) refer to the six phases of the experiment:

- (A) If the supply voltage U_0 is below the ignition voltage U_c the gas discharge will not ignite. In this phase the gas is in a dielectric state.
- (B) If the supply voltage U_0 is increased above the ignition voltage U_c a self-sustained homogeneous discharge will evolve, which is reflected by an nearly linearly increasing global current I .
- (C) At the critical voltage U_{up} the homogeneous discharge is spontaneously destabilized to a hexagonal Turing-pattern composed of current density filaments. This pattern formation is accompanied by a switch of the current-voltage-characteristic to its high-current branch.
- (D) Decreasing the supply voltage U_0 leads to the successive extinguishing of single current density filaments which is accompanied by a decrease of the discharge current I . Tuning the supply voltage even below the critical value U_{down} leads to the vanishing of the last current density filament and the system returns to its zero current branch (A).
- (E) If the supply voltage is not decreased below the critical value U_{down} , such that one current density filament (Fig. 2.11a) still remains, and the supply voltage is increased, the global current increases, too.

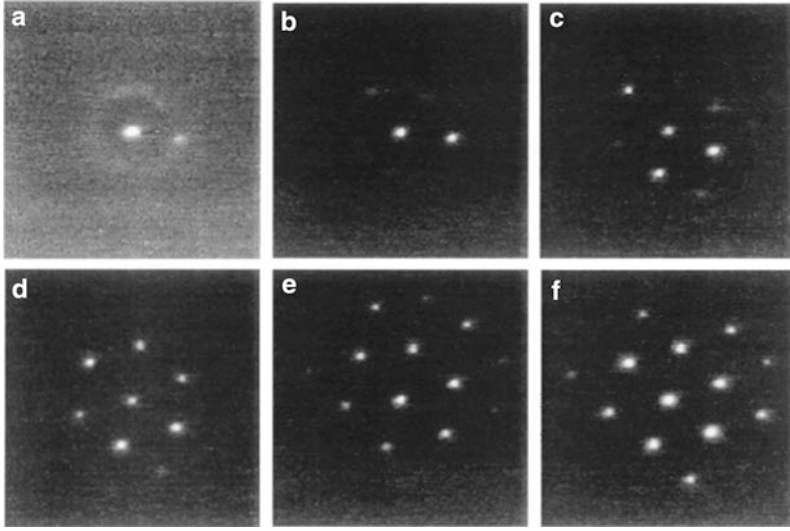


Fig. 2.11 The self-completion scenario observed from Astrov and Logvin [2.55]. (a)–(f) Luminance distribution emitted from the discharge gap for step-wise increased supply voltage U_0 at branch (F) of the current-voltage-characteristic shown in Fig. 2.10. The width of the depicted luminance distribution is 14 mm. Parameters: $U_0 \approx 3.2$ kV, no series resistor, $p_{N_2} = 150$ hPa, $d = 1.4$ mm, $a_{SC} = 450$ μ m, $t_{exp} = 40$ ms. For additional parameters see [2.55]

(F) Further increase of the control parameter above the critical value of $U_{up(1)}$ leads to the generation of new current density filaments, which is reflected by a switch of the characteristic to the high current branch. Note, that the remaining current density filament acts as a kind of seed, because the newly generated filaments ignite on its oscillating tail forming a hexagon of one central and six surrounding filaments (Fig. 2.11b–d). Additional filaments ignite on the edges of the hexagonal grid (Fig. 2.11e, f), such that a cluster of hexagonally ordered current density filaments evolves.

A similar generation process of current density filaments due to the measurement of a current-density-characteristic has been reported by Becker and Ammelt [2.65, 2.68, 2.69]. Though, it does not show the spontaneous formation of a Turing-pattern or a hexagonal cluster, but the successive ignition of current density filaments on rather arbitrary locations on the gas discharge plane, which most likely is caused by inhomogeneities of the semiconductor [2.65, S. 44]. Therefore the related current-voltage-characteristic cannot be regarded as generic. However, simulations of the self-completion scenario on isotropic domains (Sect. 7.1.3) indicate, that the experiment performed by Astrov and Logvin also had some kind of inhomogeneities e.g. due to an inhomogeneous illumination of the semiconductor. Otherwise it would not be possible to observe the successive ignition of current density filaments.

The increase of the supply voltage can also trigger a completely different generation phenomenon, the so-called self-replication, which is reported by Strümpel

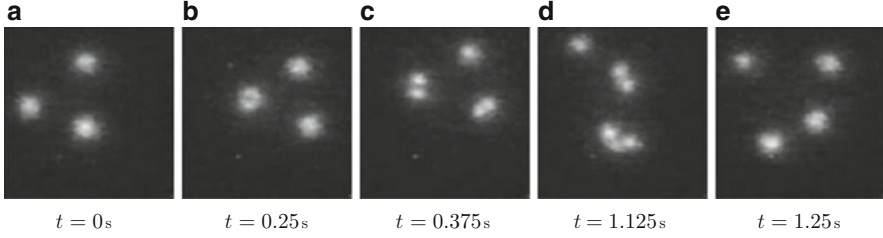


Fig. 2.12 Generation of current density filaments due to self-replication, which has been triggered by an increase of the supply voltage [2.41]. In order to realize a high specific resistivity of the Si(Pt)-semiconductor, the system has been cooled down to a temperature of $T_{SC} = 77$ K. $U_0 = 1.9$ kV, $R_0 = 41$ M Ω , $p_{N_2} = 210$ hPa, $D = 22$ mm, $d = 350$ μ m, $L_d = 4.25$ mm, $t_{exp} = 500$ μ s

[2.70, p. 99], Astrov and Purwins [2.41]. It is characterized by the spontaneous division of a dissipative soliton as depicted in Fig. 2.12. The series of snapshots shows the transition from three to four current density filaments due to a splitting process. The division obviously results from an intrinsic instability of the dissipative solitons, which becomes visible as lateral contraction of the localized structures. In simulations a similar effect is induced by a spatial inhomogeneity (Sect. 7.3.3). However, the fact that self-replication of dissipative solitons has also been observed in other self-organizing semiconductor gas discharge systems [2.70, 2.71] and chemical systems (Fig. 2.5) reflects the generic nature of the phenomenon.

2.2.3.3 Generation by Interaction

Interaction processes between dissipative solitons can also trigger the ignition of new particle-like structures. This effect is e.g. observed for ensembles of propagating dissipative solitons, which have been created by an increase of the specific conductivity of the semiconductor, if the global current is restricted due to a series resistor (cf. Fig. 2.9). For such configuration Astrov and Purwins report [2.59], that two or three current density filaments are able to generate another filament, if their distance drops below a characteristic critical value (Fig. 2.13). The newly generated dissipative soliton is also a stable entity and instantly starts to interact with its neighbored dissipative solitons. However, this interaction does not trigger a chain reaction due to the series resistor which restricts the global current. On the other hand the ignition of new dissipative solitons due to interaction processes becomes more likely, if other current density filaments have been annihilated, e.g. due to an interaction process with the boundary of the active area.

Obviously this so-called *replication* process bears some similarity to the later state of the self-completion phenomena (Fig. 2.11c–f) at which the additional filaments ignite in a characteristic distance to the already existing ones. Indeed both phenomena can be related to the same mechanism, viz. the superposition of oscillating tails of the localized structures (Sect. 7.4.2).

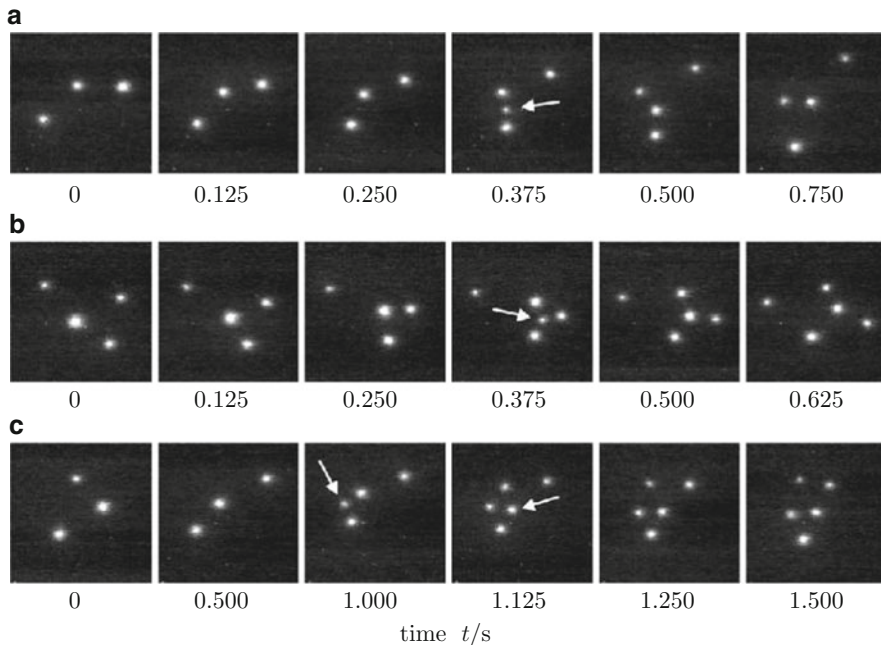


Fig. 2.13 The replication of current density filaments due to the interaction of two (a) or three (b) and (c) dissipative solitons [2.59]. The arrow indicates the generated filament. Parameters correspond to Fig. 2.9e

2.2.3.4 Annihilation by Interaction

Complementary to the generation of current density filaments is their annihilation, which is observed in two different variants: Annihilation by fading and annihilation by merging. While the latter is clearly identified as a two-particle process the fading of filaments occurs typically in significant distance to other filaments [2.70, S. 102], such that mutual interaction with other dissipative solitons can be neglected. If the fading occurs close to the boundary of the active area a collision with the boundary is most likely the cause of the annihilation.

In order to give an illustrative example of the rarely observed merging of current density filaments, Fig. 2.14 visualizes an experimental observation of Bödeker [2.72, 2.73]. The subfigures show negatives of the luminance distribution in order to present the details of the process with optimal contrast. Two current density filaments approach each other (Fig. 2.14a) and merge to a transient state with high local current density (Fig. 2.14b, c). This transient state decays to a single dissipative soliton in the range of milliseconds (Fig. 2.14d), such that the number of dissipative solitons effectively has been reduced by one.

Note, that the system is not stable in the presented scenario, if only one current density filament exists. Therefore a new filament will shortly ignite after

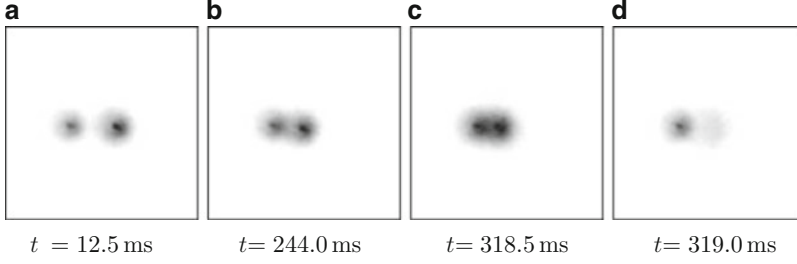


Fig. 2.14 Annihilation by merging. The snapshots are negatives of the luminance distribution recorded by Bödeker [2.72, p. 38]. **(a)** Approaching current density filaments. **(b)** and **(c)** Merging of current density filaments to transient state. **(d)** Reconfiguration to single current density filament. Parameters: $L_d = 8$ mm, $U_0 = 3.8$ kV, $\rho_{SC} = 4.14$ M $\Omega \cdot$ cm, $R_0 = 20$ M Ω , semiconductor GaAs(Cr), $p_{N_2} = 290$ hPa, $T_{SC} = 100$ K, $D = 17$ mm, $d = 500$ μ m, $a_{SC} = 1.0$ mm, $t_{exp} = 0.4$ ms, $f_{rep} = 2$ kHz

an annihilation has occurred. A similar interplay between generation and annihilation has been observed in the many-particle system presented in Fig. 2.9e. Here annihilation is mainly caused by collisions with the boundary of the active area and therefore can be regarded as annihilation by fading.

2.2.4 Dynamics

For certain experimental parameters only a single or a few current density filaments exist within the active area of the semiconductor gas-discharge-system. If the electrodes have been prepared with sufficient homogeneity, the current density filaments will move on irregular paths indicating a significant influence of noise. However, the experimenter will quickly observe, that for some experimental parameters the filaments seem to be less influenced by noise than for other parameter sets.

In order to visualize these differences the position $\mathbf{p}(t)$ of the current density filaments has to be extracted from a set of recorded luminance distributions $\phi(\mathbf{x}, t_j)$. For this purpose a threshold ϕ_T is chosen, which separates the luminance distribution $\phi(\mathbf{x}, t)$ into a subarea $\{\phi(\mathbf{x}, t) | \phi(\mathbf{x}, t) \geq \phi_T\}$ of increased luminosity, which indicates the existence of a current density filament, and the embedding background discharge [2.74]. Having this threshold ϕ_T at hand the position $\mathbf{p}(t)$ of the dissipative soliton can be computed from

$$\mathbf{p}(t) = \frac{\int_{\{\mathbf{x} | \phi(\mathbf{x}, t) \geq \phi_T\}} \mathbf{x} \phi(\mathbf{x}, t) d\mathbf{x}}{\int_{\{\mathbf{x} | \phi(\mathbf{x}, t) \geq \phi_T\}} \phi(\mathbf{x}, t) d\mathbf{x}}. \quad (2.2)$$

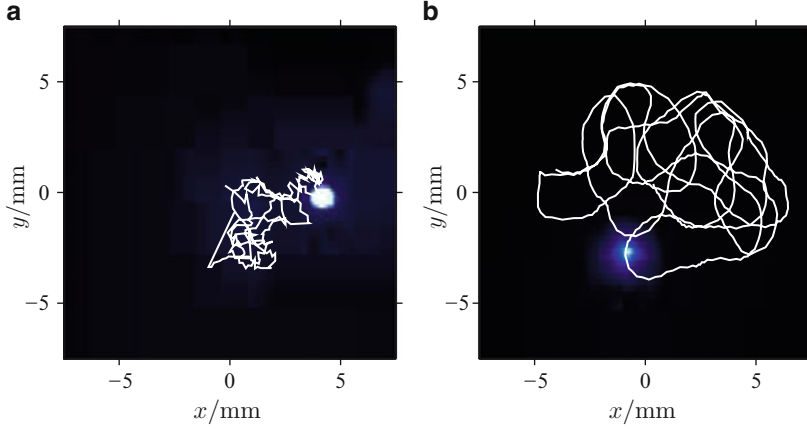


Fig. 2.15 Dynamics of current density filaments [2.61]. The subfigures show a snapshot of the luminosity emitted from the discharge gap. Superimposed to the false colour representation of the luminosity are trajectories of the localized structures. **(a)** Trajectory of the current density filament for 31 s. Parameters: $U_0 = 3.60$ kV, $\rho_{SC} = 2.02$ M $\Omega \cdot$ cm, $R_0 = 10$ M Ω , $I = 116$ μ A, semiconductor GaAs(Cr), $p_{N_2} = 280$ hPa, $T_{SC} = 100$ K, $D = 17$ mm, $d = 550$ μ m, $a_{SC} = 1.0$ mm, $t_{exp} = 20$ ms, $f_{rep} = 50$ Hz. **(b)** Trajectory of the current density filament for 39 s. Parameters from Fig. 2.8a

If several dissipative solitons exist simultaneously on the active area the threshold has to assure, that each localized structure i can be assigned a unique position $\mathbf{p}_i(t)$. For the experimentally recorded trajectories presented in this work the analysis has been performed by the programs FilaCount and FilaTrace [2.75].

Two typical filament trajectories $\mathbf{p}(t)$ are visualized in Fig. 2.15a, b. Each subfigure shows a snapshot of the luminance distribution $\phi(x, y)$ with the corresponding filament trajectory. They visualize the different types of motion observed experimentally. While the trajectory of Fig. 2.15a is characterized by frequent random changes of the direction of motion, the trajectory of Fig. 2.15b represents a relative smooth motion with less frequent changes of the direction of motion.

These observations lead to the question, whether the qualitative differences of the dynamics of current density filaments are caused by an intrinsic property of the self-organized structures. This question is considered in Sect. 6 by introducing a stochastic time series analysis, which is capable of separating the deterministic and the stochastic part of the dynamics.

2.2.5 Interaction Processes with Conservation of the Number of Dissipative Solitons

Up to now the particle-like character of dissipative solitons has been discussed on basis of experimental results, which show the generation or annihilation of these self-organized entities as a whole in the course of two- or many-particle

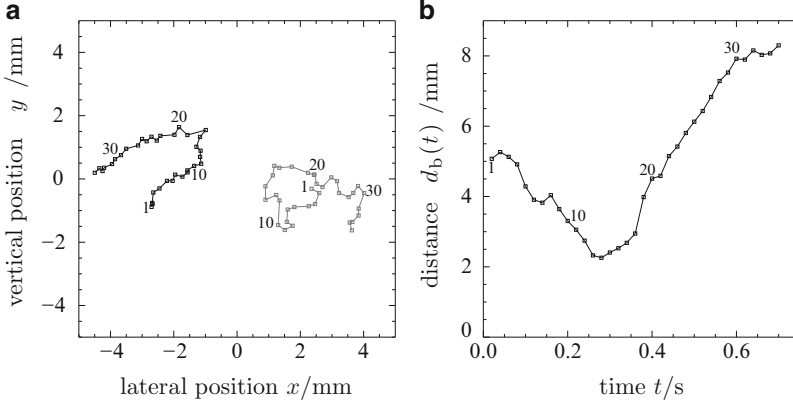


Fig. 2.16 Scattering of two dissipative solitons [2.52]. *Numbers* reference the respective snapshots. **(a)** Trajectories $\mathbf{p}_i(t)$ extracted from the recorded luminance distribution. The symbols are enumerated with respect to the snapshot from which the positions have been extracted. **(b)** Time series of particle distance $d_b(t) = |\mathbf{p}_2(t) - \mathbf{p}_1(t)|$. Parameters: $U_0 = 3.7$ kV, $\rho_{SC} = 1.52$ M Ω ·cm, $R_0 = 4.4$ M Ω , $I = 300$ μ A, semiconductor GaAs(Cr), $p_{N_2} = 270$ hPa, $T_{SC} = 100$ K, $D = 20$ mm, $d = 500$ μ m, $a_{SC} = 1.0$ mm, $t_{exp} = 20$ ms, $f_{rep} = 50$ Hz

interactions. Another important aspect of their particle-like properties is the ability to interact with each other while the number of interacting dissipative solitons is preserved. The following sections document this ability on basis of experimentally observed scattering events (Sect. 2.2.5.1), the formation of transient bound states (Sect. 2.2.5.2), the dynamics of rotating bound states (Sect. 2.2.5.3), and many particle phenomena (Sect. 2.2.5.4). These observations act as motivation for the theoretical considerations conducted in Chap. 5.

2.2.5.1 Scattering

A good example for demonstrating the particle-like character of dissipative solitons are scattering processes, where the motion of individual dissipative solitons is affected by the attractive or repulsive interaction of other dissipative solitons without being captured in transient bound states. In such scenarios the dissipative solitons approach each other up to a distinct distance, such that the merging of dissipative solitons cannot occur. Note, that the scattering distance is a typical characteristic of interaction processes for a chosen set of experimental parameters. Such kind of interaction is shown in Fig. 2.16 as trajectories $\mathbf{p}_1(t)$ and $\mathbf{p}_2(t)$ of their luminance distribution (Fig. 2.16a), which have been computed from (2.2). Additionally Fig. 2.16b shows the distance $d_b(t) = |\mathbf{p}_2(t) - \mathbf{p}_1(t)|$ of the interacting dissipative solitons. The symbols of both plots are enumerated with respect to the number of the recorded luminance distribution, from which the positions have been extracted. Despite the fluctuations it can be seen from the plots, that the dissipative

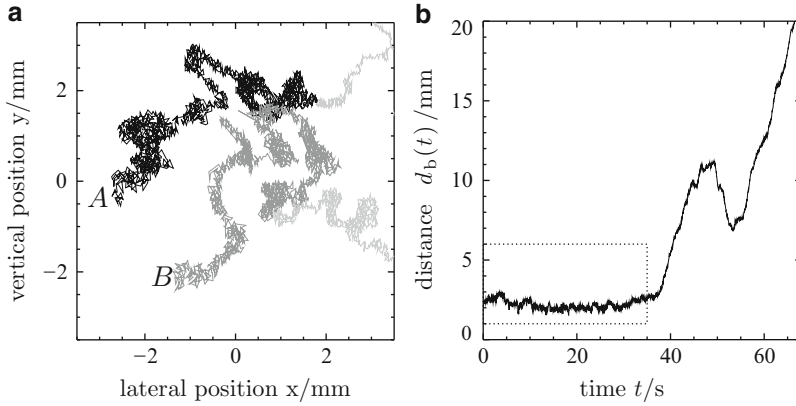


Fig. 2.17 Transient bound state of two dissipative solitons [2.52]. (a) Trajectories $p_i(t)$ computed from the respective luminance distributions. *Black* and *dark gray* lines indicate trajectories of the first 35 s, where the dissipative solitons are considered as being bound. *Light gray* lines indicate trajectories for $t > 35$ s. (b) Distance $d_b(t)$ of the dissipative solitons. Parameters: $U_0 = 3.1$ kV, $\rho_{SC} = 4.19 \text{ M}\Omega \cdot \text{cm}$, $R_0 = 4.4 \text{ M}\Omega$, $I = 170 \text{ }\mu\text{A}$, semiconductor GaAs(Cr), $p_{N_2} = 280 \text{ hPa}$, $T_{SC} = 100 \text{ K}$, $D = 20 \text{ mm}$, $d = 450 \text{ }\mu\text{m}$, $a_{SC} = 1.0 \text{ mm}$, $t_{exp} = 50 \text{ ms}$

solitons approach each other up to a closest distance at the 14th snapshot, when the mutual repulsion enforces a change of direction, such that the dissipative solitons veer away from each other.

2.2.5.2 Transient Bound States

One of the most astonishing property of current density filaments is the fact, that they are able to build bound states. These are characterized by a distinct binding distance between the bound filaments. In most cases the bound state decays within a short time interval after its formation into two independent filaments due to external fluctuations. A typical example for such kind of bound state is shown in Fig. 2.17 on basis of two particle trajectories (Fig. 2.17a) and the evolution of the distance between these solitary objects (Fig. 2.17b). The plotted trajectories start at positions A and B corresponding to $t = 0$ in Fig. 2.17b, when the bound state already has formed. Obviously the dynamics act on two different time scales: A fast time scale reflecting the stochastic dynamics of the individual dissipative soliton and a slow time scale on which the bound state propagates. Fluctuations of the fast time scale become visible in Fig. 2.17b as short term fluctuations of the distance between the dissipative solitons. Within the first 37 s of the recording the binding distance fluctuates around a mean value of $(2.2 \pm 0.3) \text{ mm}$. Contrary to this obviously stabilized binding is the break-up of the bound state at $t \approx 37$ s, which leads to a rapid separation of the filaments (Fig. 2.17b). Only the beginning of this separation is shown in Fig. 2.17a, which covers approximately the first 40 s of the distance plot.

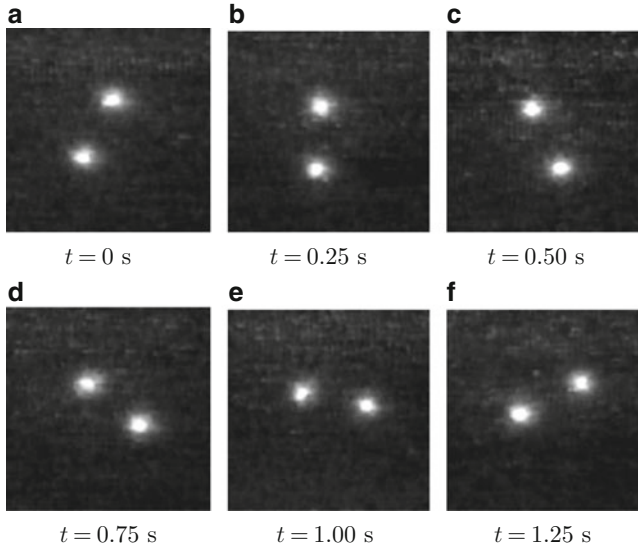


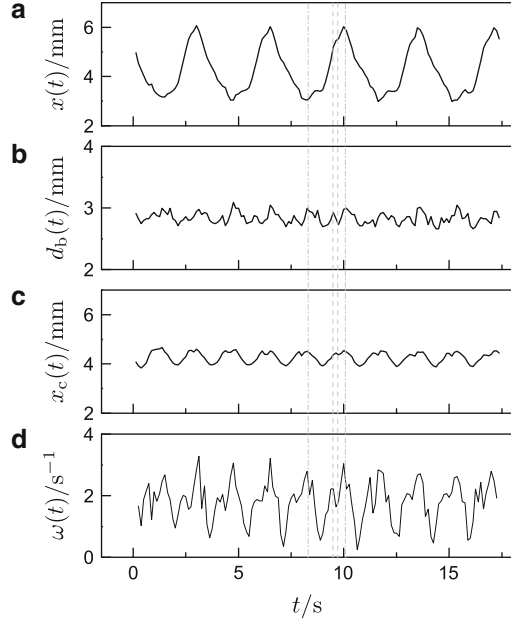
Fig. 2.18 Rotating bound state of two dissipative solitons observed in the semiconductor gas-discharge system [2.62]. The images show the luminance distributions of the counterclockwise rotating structure covering approximately a rotation of 180° . Parameters: $L_d = 9$ mm, $U_0 = 1.9$ kV, $\rho_{SC} = 22.2$ M $\Omega \cdot$ cm, $R_0 = 5$ M Ω , $I = 3.2$ μ A, semiconductor Si(Zn), $p_{N_2} = 200$ hPa, $T_{SC} = 90$ K, $d = 0.8$ mm, $a_{SC} = 1.0$ mm, $D = 20$ mm, $t_{exp} < 0.01$ s

The stabilized binding on the one hand and the rapid increase of distance on the other hand indicate a special kind of interaction, which changes from attraction to repulsion in dependency of the interaction distance. Historically such kind of interaction had been an important attempt for explaining the complex structures found in inanimate nature since the eighteenth century [2.76, 2.77], which had only been discarded due to the success of modern physics at the beginning of the twentieth century. However, in dissipative systems this is the most important type of interaction between self-organized structures, which is discussed in detail in Chap. 5.

2.2.5.3 Rotating Structures

In Sect. 2.2.3 the self-completion scenario has been introduced, which is suitable for generating small clusters of dissipative solitons. This mechanism has been applied for generating a rotating cluster of two dissipative solitons by starting with a propagating current density filament and increasing the supply voltage until a second filaments ignites in direct neighbourhood to the first one. The resulting structure is shown in Fig. 2.18. Obviously the two current density filaments form a bound state, which rotates counterclockwise. Further increase of the supply voltage results in

Fig. 2.19 Dynamics of the rotating bound state depicted in Fig. 2.18 [2.62]. Gray vertical lines indicate the correlations between the different time series. They mark significant discontinuities of the dynamics within one half period of rotation. (a) Projection of position $\mathbf{p}(t)$ of the *upper right* dissipative soliton depicted in Fig. 2.18a on the x -axis. (b) Distance $d_b(t)$ between the rotating dissipative solitons. (c) Projection of the *center* $\mathbf{p}_c(t)$ of the bound state on the x -axis. (d) Angular velocity $\omega(t)$ of the bound state



the ignition of additional current density filaments and a much more complicated dynamics of the resulting cluster, which should not be discussed here. The detailed examination of the observed dynamics is visualized in Fig. 2.19. The discussion starts with the time series of the x -coordinate of the upper right dissipative soliton depicted in Fig. 2.18a. In Fig. 2.19a its x -coordinate has been plotted for five rotations. The curve shows a repeated pattern with significant deviations from the sinusoidal form. Notably, the deviations are replicated for each rotation, which indicates the influence of spatial inhomogeneities.

The time series of the distance $d_b(t)$ between the dissipative solitons is shown in Fig. 2.19b for the same time interval. The distance $d_b(t)$ fluctuates characteristically around the mean distance of (2.836 ± 0.093) mm with half the period observed for $x(t)$. This is caused by the fact, that both dissipative solitons are identical and are identically influenced by the spatial inhomogeneities.

Defining the center $\mathbf{p}_c(t) = (x_c(t), y_c(t))^T$ of the bound state as the midpoint of the connecting line between the centers of both luminosity distributions, another characteristic time series $x_c(t)$ can be examined (Fig. 2.19c). Its curve shows the same periodicity as the distance $d_b(t)$ and a fine structure, which is obviously correlated to the fine structure of $x(t)$. Additionally one observes, that the fluctuations of the center of the cluster are accompanied by strong fluctuations of the angular velocity $\omega(t)$ of the cluster (Fig. 2.19d).

The observation indicates, that bound states of dissipative solitons do not need to be transient (Sect. 2.2.5.2) but also exist as stable states. However, in the presented scenario the dynamics of the rotating bound state is strongly influenced

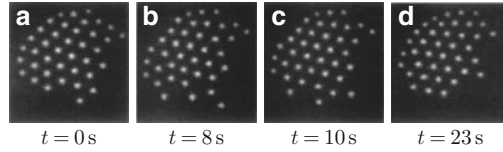


Fig. 2.20 Many particle system with constant number of dissipative solitons [2.55]. (a)–(d) Snapshots of the luminance distribution for constant parameters: $U_0 = 1,900$ V, $p_{N_2} = 130$ hPa, $T_{SC} \approx 90$ K, $d = 0.8$ mm, $a_{SC} = 1.0$ mm, $D = 20$ mm, for additional parameters see [2.55]

by spatial inhomogeneities, which are presumably located at the semiconductor. The inhomogeneities excite internal degrees of freedom such that the binding distance is not constant.

Note, that the distance between both dissipative solitons is small compared to the distance of the filaments to the boundary of the active area, such that the boundary does not stabilize the structure or influences its dynamics. This is in contrast to the observation of rotating hexagonal patterns on circular domains as reported for combustion experiments [2.78, 2.79] or ac-driven gas-discharge systems [2.80], for which the rotational dynamics is determined by the circular shape of the domain and the related breaking of symmetry. However, rotating bound states of dissipative solitons, which are not stabilized by the boundary of the system, are for example observed for oil droplets on a bath of silicon oil which is oscillated vertically [2.81–2.83].

2.2.5.4 Many Particle Phenomena

In Sect. 2.2.3.1 a many particle phenomena has been introduced, where the number of dissipative solitons varies due to repeated generation and annihilation processes. Comparable results are also obtained for experimental parameters without generation and annihilation processes of dissipative solitons. In these cases the number of dissipative solitons is constant, but the ordering of the clusters varies due to the stochastic dynamics of the system.

An example for such kind of phenomena is shown in Fig. 2.20. The figure shows four snapshots of the luminosity distribution emitted from 39 current density filaments, which have been generated due to a self-completion scenario (Sect. 2.2.3). However, the number of dissipative solitons is constant, because the system parameters are not changed and does not permit the annihilation or generation of particles due to interaction processes.

The series of snapshots shows a cluster of hexagonally ordered current density filaments, which is not rigid but allows for the relocation of single dissipative solitons at the boundaries of the cluster. On the time scale of several seconds the consecutive process of detaching and reconnecting of single dissipative solitons leads to the restructuring of the cluster. Astrov and Logvin interpret this observation

as noise induced evaporation and condensation of individual dissipative solitons [2.55], at which the hexagonally ordered state is identified as condensed phase.

References

- 2.1. G. Wald, Nobel Lect. Physiol. Med. **4**, 255 (1967)
- 2.2. V. Castets, E. Dulos, J. Boissonade, P. De Kepper, Phys. Rev. Lett. **64**(24), 2953 (1990). doi:10.1103/PhysRevLett.64.2953
- 2.3. A. Mikhailov, K. Showalter, Phys. Rep. **425**(2–3), 79 (2006). doi:10.1016/j.physrep.2005.11.003
- 2.4. V.K. Vanag, I.R. Epstein, Chaos **18**(2), 026107 (2008). doi:10.1063/1.2900555
- 2.5. H.H. Rotermund, S. Jakubith, A. von Oertzen, G. Ertl, Phys. Rev. Lett. **66**(23), 3083 (1991). doi:10.1103/PhysRevLett.66.3083. Copyright 1991 by the American Physical Society
- 2.6. K.J. Lee, W.D. McCormick, J.E. Pearson, H.L. Swinney, Nature **369**, 215 (1994). doi:10.1038/369215a0
- 2.7. D.G. Míguez, V.K. Vanag, I.R. Epstein, Proc. Natl. Acad. Sci. USA **104**(17), 6992 (2007). doi:10.1073/pnas.0611438104
- 2.8. W. Engel, M. Kordesch, H. Rotermund, S. Kubala, A. von Oertzen, Ultramicroscopy **36**(1–3), 148 (1991). doi:10.1016/0304-3991(91)90146-W
- 2.9. K. Asakura, J. Lauterbach, H.H. Rotermund, G. Ertl, J. Chem. Phys. **102**(20), 8175 (1995). doi:10.1063/1.469229
- 2.10. J. Christoph, M. Eiswirth, N. Hartmann, R. Imbühl, I. Kevrekidis, M. Bär, Phys. Rev. Lett. **82**(7), 1586 (1999). doi:10.1103/PhysRevLett.82.1586
- 2.11. S.Y. Yamamoto, C.M. Surko, M.B. Pina, Phys. Rev. Lett. **74**(20), 4071 (1995). doi:10.1103/PhysRevLett.74.4071
- 2.12. B.P. Belousov, in *Compilation of Abstracts on Radiation Medicine* (Medgiz, Moscow, 1959), pp. 145–152. In Russian
- 2.13. A.M. Zhabotinsky, Biofizika **9**, 306 (1964). In Russian
- 2.14. A.N. Zaikin, A.M. Zhabotinsky, Nature **225**, 535 (1970). doi:10.1038/225535b0
- 2.15. A.T. Winfree, Science **175**, 634 (1972)
- 2.16. A.M. Zhabotinsky, A.N. Zaikin, J. Theor. Biol. **40**(1), 45 (1973). doi:10.1016/0022-5193(73)90164-1
- 2.17. L. Kuhnert, Nature **319**, 393 (1986). doi:10.1038/319393a0
- 2.18. E. Mihaliuk, T. Sakurai, F. Chirila, K. Showalter, Faraday Discuss. **120**, 383 (2002). doi:10.1039/b103431f. Reproduced by permission of The Royal Society of Chemistry.
- 2.19. E. Mihaliuk, T. Sakurai, F. Chirila, K. Showalter, Phys. Rev. E **65**(6), 065602 (2002). doi:10.1103/PhysRevE.65.065602
- 2.20. S. Kádár, J. Wang, K. Showalter, Nature **391**, 770 (1998). doi:10.1038/35814
- 2.21. V.K. Vanag, L. Yang, M. Dolnik, A.M. Zhabotinsky, I.R. Epstein, Nature **406**, 389 (2000). doi:10.1038/35019038
- 2.22. I. Sendina-Nadal, E. Mihaliuk, J. Wang, V. Perez-Munuzuri, K. Showalter, Phys. Rev. Lett. **86**(8), 1646 (2001)
- 2.23. T. Sakurai, E. Mihaliuk, F. Chirila, K. Showalter, Science **296**(5575), 2009 (2002). doi:10.1126/science.1071265
- 2.24. A.J. Steele, M. Tinsley, K. Showalter, Chaos **18**(2), 026108 (2008). doi:10.1063/1.2900386
- 2.25. M.R. Tinsley, A.J. Steele, K. Showalter, Eur. Phys. J. **165**, 161 (2008). doi:10.1140/epjst/e2008-00859-7
- 2.26. A.M. Turing, Philos. Trans. R. Soc. B **237**, 37 (1952)
- 2.27. Z. Zoszticzius, W. Hosrthemke, W.D. McCormick, H.L. Swinney, W.Y. Tam, Nature **329**, 619 (1987). doi:10.1038/329619a0

- 2.28. Q. Ouyang, V. Castets, J. Boissonade, J.C. Roux, P.D. Kepper, H.L. Swinney, J. Chem. Phys. **95**(1), 351 (1991)
- 2.29. Q. Ouyang, H.L. Swinney, Nature **352**, 610 (1991). doi:10.1038/352610a0
- 2.30. V.K. Vanag, I.R. Epstein, Phys. Rev. Lett. **87**(22), 228301 (2001). doi:10.1103/PhysRevLett.87.228301
- 2.31. R.J. Field, E. Körös, R.M. Noyes, J. Am. Chem. Soc. **94**(25), 8649 (1972). doi:10.1021/ja00780a001
- 2.32. R.J. Field, R.M. Noyes, J. Chem. Phys. **60**(5), 1877 (1974)
- 2.33. V.K. Vanag, I.R. Epstein, Patterns of nanodroplets: the Belousov-Zhabotinsky-aerosol OT-microemulsion system, in *Self-Organized Morphology in Nanostructured Materials*. Springer Series in Materials Science, vol. 99 (Springer, Heidelberg, 2008), pp. 89–113. doi:10.1007/978-3-540-72675-3_5
- 2.34. A. Kaminaga, V.K. Vanag, I.R. Epstein, J. Chem. Phys. **122**, 174706 (2005). doi:10.1063/1.1888386
- 2.35. A. Kaminaga, V.K. Vanag, I.R. Epstein, Angew. Chem. Int. Ed. **45**, 3087 (2006). doi:10.1002/anie.200600400
- 2.36. V.K. Vanag, I.R. Epstein, Phys. Rev. Lett. **92**(12), 128301 (2004). doi:10.1103/PhysRevLett.92.128301
- 2.37. K.J. Lee, W.D. McCormick, Q. Ouyang, H.L. Swinney, Science **261**(5118), 192 (1993). doi:10.1126/science.261.5118.192
- 2.38. R.D. Vigil, Q. Ouyang, H.L. Swinney, Phys. A **188**, 17 (1992)
- 2.39. I. Szalai, P.D. Kepper, J. Phys. Chem. A **112**(5), 783 (2008). doi:10.1021/jp711849m
- 2.40. I. Szalai, P.D. Kepper, Chaos Interdiscip. J. Nonlinear Sci. **18**(2), 026105 (2008). doi:10.1063/1.2912719. <http://link.aip.org/link/?CHA/18/026105/1>. Copyright 2008, American Institute of Physics
- 2.41. Yu.A. Astrov, H.-G. Purwins, Phys. Lett. A **358**, 404 (2006). doi:10.1016/j.physleta.2006.05.047. Fig. 2.12 published with kind permission of Elsevier. Copyright (2006)
- 2.42. K.J. Lee, W.D. McCormick, J.E. Pearson, H.L. Swinney, Nature **369**, 215 (1994). doi:10.1038/369215a0
- 2.43. G. Li, Q. Ouyang, H.L. Swinney, J. Chem. Phys. **105**(24), 10830 (1996). doi:10.1063/1.472891
- 2.44. T.C. Lengnick, Discharge tube. Patent 1,936,514, United States Patent Office (1933)
- 2.45. S.S. Kasimov, L.G. Paritskii, S.M. Rivkin, Investigation of the ionization-type image converter. VINITI N2693-74 (1974). In Russian
- 2.46. Yu.A. Astrov, L.M. Portsel, S.P. Teperick, H. Willebrand, H.-G. Purwins, J. Appl. Phys. **74**(4), 2159 (1993)
- 2.47. L.M. Portsel, Yu.A. Astrov, I. Reimann, E. Ammelt, H.-G. Purwins, J. Appl. Phys. **85**, 3960 (1999)
- 2.48. J.H.R. Kim, H. Maurer, Yu.A. Astrov, M. Bode, H.-G. Purwins, J. Comput. Phys. **170**, 395 (2001)
- 2.49. V.M. Marchenko, S. Matern, Yu.A. Astrov, L.M. Portsel, H.-G. Purwins, Proc. SPIE **4669**, 1 (2002)
- 2.50. S. Matern, V.M. Marchenko, Yu.A. Astrov, L.M. Portsel, H.-G. Purwins, Proc. SPIE **4669**, 13 (2002)
- 2.51. S. Matern, V.M. Marchenko, Yu.A. Astrov, L.M. Portsel, H.-G. Purwins, Photonik **3**, 84 (2002)
- 2.52. H. Bödeker, A.W. Liehr, T.D. Frank, R. Friedrich, H.-G. Purwins, New J. Phys. **6**(62), 1 (2004). Published with kind permission of IOP Publishing Ltd
- 2.53. E. Ammelt, Yu.A. Astrov, H.-G. Purwins, Phys. Rev. E **58**(6), 7109 (1998)
- 2.54. Yu.A. Astrov, E. Ammelt, S. Teperick, H.-G. Purwins, Phys. Lett. A **211**(3), 184 (1996)
- 2.55. Yu.A. Astrov, Yu.A. Logvin, Phys. Rev. Lett. **79**(16), 2983 (1997). Figs. 2.10, 2.11, and 2.20 published with kind permission of the American Physical Society. Copyright (1997)
- 2.56. E.L. Gurevich, A.S. Moskalenko, A.L. Zanin, Yu.A. Astrov, H.-G. Purwins, Phys. Lett. A **307**(5–6), 299 (2003)

- 2.57. Yu.A. Astrov, E. Ammelt, H.-G. Purwins, Phys. Rev. Lett. **78**(16), 3129 (1997)
- 2.58. Yu.A. Astrov, I. Müller, E. Ammelt, H.-G. Purwins, Phys. Rev. Lett. **24**(15), 5341 (1998)
- 2.59. Yu.A. Astrov, H.-G. Purwins, Phys. Lett. A **283**, 349 (2001). Figs. 2.9 and 2.13 published with kind permission of Elsevier. Copyright (2001)
- 2.60. H. Bödeker, M.C. Röttger, A.W. Liehr, T. Frank, R. Friedrich, H.-G. Purwins, Phys. Rev. E **67**(056220), 1 (2003). doi:10.1103/PhysRevE.67.056220
- 2.61. A.W. Liehr, H.U. Bödeker, M.C. Röttger, T.D. Frank, R. Friedrich, H.-G. Purwins, New J. Phys. **5**(89), 1 (2003). <http://stacks.iop.org/1367-2630/5/89>. Published with kind permission of IOP Publishing Ltd
- 2.62. A.W. Liehr, A.S. Moskalenko, Yu.A. Astrov, M. Bode, H.-G. Purwins, Eur. Phys. J. B **37**, 199 (2004). Figs. published with kind permission of EDP Sciences
- 2.63. C. Strümpel, H.-G. Purwins, Yu.A. Astrov, Phys. Rev. E **63**(2), 026409/1 (2001)
- 2.64. C. Strümpel, Yu.A. Astrov, H.-G. Purwins, Phys. Rev. E **65**(066210), 1 (2002)
- 2.65. D. Becker, Frontausbreitung und Filamentstrukturen in einem zweidimensionalen gleichspannungsbetriebenen Gasentladungssystem. Master's thesis, Institut für Angewandte Physik, Westfälische Wilhelms-Universität Münster, 1994
- 2.66. S.V. Gurevich, H.U. Bödeker, A.S. Moskalenko, A.W. Liehr, H.-G. Purwins, Phys. D **199**(1–2), 115 (2004). doi:10.1016/j.physd.2004.08.020
- 2.67. H. Meinhardt, A. Gierer, J. Cell Sci. **15**, 321 (1974)
- 2.68. E. Ammelt, Untersuchungen zur Strukturbildung in planaren Gasentladungssystemen mit bildverarbeitenden Methoden. Dissertation, Institut für Angewandte Physik, Westfälische Wilhelms-Universität Münster, 1994
- 2.69. H.-G. Purwins, AIP Conf. Proc. **993**(1), 67 (2008). doi:10.1063/1.2909178. <http://link.aip.org/link/?APC/993/67/1>
- 2.70. J.C. Strümpel, Experimentelle Untersuchung der raumzeitlichen Strukturierung in einem planaren Halbleiter-Gasentladungssystem. Dissertation, Institut für Angewandte Physik, Westfälische Wilhelms-Universität Münster, 2001
- 2.71. H. Willebrand, F.-J. Niedernostheide, E. Ammelt, R. Dohmen, H.-G. Purwins, Phys. Lett. A **153**(8), 437 (1991)
- 2.72. H.U. Bödeker, Dynamik und Wechselwirkung dissipativer Solitonen in einer planaren Gleichspannungs-Gasentladung. Master's thesis, Institut für Angewandte Physik, Westfälische Wilhelms-Universität Münster, 2003
- 2.73. H.-G. Purwins, H.U. Bödeker, A.W. Liehr, in *Dissipative Solitons*, ed. by N. Akhmediev, A. Ankiewicz (Springer, Berlin, 2005), pp. 267–308
- 2.74. J.C. Russ, *The Image Processing Handbook*, 4th edn. (CRC, Boca Raton, 2002)
- 2.75. S. Flothkötter, Untersuchung laufender Stromfilamente in einem Si{Zn}-Hybrid-Gasentladungssystem. Master's thesis, Institut für Angewandte Physik, Westfälische Wilhelms-Universität Münster, 2001
- 2.76. P.R.J. Boscovich, *Theoria philosophiae naturalis. Redacta ad unicam legem virium in natura existentium* (Remondiniana, Venedig, 1763)
- 2.77. R.J. Boscovich, *A Theory of Natural Philosophy. English Edition from the Text of the First Venetian Edition Published Under the Personal Superintendence of the Author in 1763* (MIT, Cambridge, 1966)
- 2.78. G.H. Gunaratne, M. El-Hamdi, M. Gorman, Mod. Phys. Lett. B **10**(28), 1379 (1996)
- 2.79. A. Palacios, G.H. Gunaratne, M. Gorman, K.A. Robbins, Chaos **7**(3), 463 (1997)
- 2.80. A.L. Zanin, E.L. Gurevich, A.S. Moskalenko, H.U. Bödeker, H.-G. Purwins, Phys. Rev. E **70**(3), 036202 (2004). doi:10.1103/PhysRevE.70.036202
- 2.81. Y. Couder, S. Protiere, E. Fort, A. Boudaoud, Nature **437**(7056), 208 (2005). doi:10.1038/437208a
- 2.82. S. Protiere, Y. Couder, E. Fort, A. Boudaoud, J. Phys. Condens. Matter **17**(45), S3529 (2005). doi:10.1088/0953-8984/17/45/044
- 2.83. S. Protiere, A. Boudaoud, Y. Couder, J. Fluid Mech. **554**(7056), 85 (2006). doi:10.1017/S0022112006009190



<http://www.springer.com/978-3-642-31250-2>

Dissipative Solitons in Reaction Diffusion Systems
Mechanisms, Dynamics, Interaction

Liehr, A.

2013, XIX, 212 p., Hardcover

ISBN: 978-3-642-31250-2